

Article

Fabrication of Sn(IV)porphyrin-Imbedded Silica Aerogel Composite

Min-Gyeong Jo, Nam-Gil Kim and Hee-Joon Kim * Department of Chemistry and Bioscience, Kumoh National Institute of Technology,
Gumi 39177, Republic of Korea

* Correspondence: hjk@kumoh.ac.kr

Abstract: Optoelectronic functional composite materials with porous structures are of great importance in various fields. A hybrid composite (SnP@SiA) composed of (*trans*-dihydroxo)(5,10,15,20-tetraphenylporphyrinato)tin(IV) (SnP) in silica aerogel (SiA) was successfully fabricated through the reaction of SnP with silanol groups of SiA in the presence of hexamethyldisilazane (HMDS). SnP@SiA was then characterized using various instrumental techniques. The zeta potential for SnP@SiA (−11.62 mV) was found to be less negative than that for SiA (−18.26 mV), indicating that the surface of SnP@SiA is covered by hydrophobic species such as SnP and trimethylsilyl groups. The Brunauer–Emmett–Teller (BET) surface area, pore volume, and average pore size of SnP@SiA are 697.07 m²/g, 1.69 cm³/g, and 8.45 nm, respectively, making it a suitable composite for catalytic applications. SnP@SiA, a photocatalyst with high porosity and a large surface area, yields promising performance in the photodegradation of acid orange 7 (AO7) under visible light irradiation in aqueous solution. This hybrid composite exhibited the desirable properties of aerogels along with the photoelectronic features of porphyrins. Therefore, this porphyrin-imbedded mesoporous material has valuable potential in various applications such as photocatalysis, light energy conversion, biochemical sensors, and gas storage.

Keywords: Sn(IV)porphyrin; silica; aerogel; porous structure; hybrid composite



Citation: Jo, M.-G.; Kim, N.-G.; Kim, H.-J. Fabrication of Sn(IV)porphyrin-Imbedded Silica Aerogel Composite. *J. Compos. Sci.* **2023**, *7*, 401. <https://doi.org/10.3390/jcs7090401>

Academic Editor: Francesco Tornabene

Received: 25 August 2023

Revised: 15 September 2023

Accepted: 19 September 2023

Published: 20 September 2023



Copyright: © 2023 by the authors. Licensee MDPI, Basel, Switzerland. This article is an open access article distributed under the terms and conditions of the Creative Commons Attribution (CC BY) license (<https://creativecommons.org/licenses/by/4.0/>).

1. Introduction

Porous materials have received considerable attention due to their valuable features, including excellent thermal and chemical stability, large accessible surface area, insoluble backbone, tunable porosity, and versatile functionality. The porosity of these materials not only increases catalytic activity by increasing the number of reactant-accessible catalyst sites, but also increases the rate of catalytic reactions by adsorbing reactant molecules. Among various porous materials, aerogels have attracted particular attention for practical applications. Aerogels are cohesive, porous solids created by forming a colloidal gel and then removing molecules trapped within the pores without significant disruption of the gel structure [1]. They are generally of very-low density and can be made in large pieces with monolithic structures [2]. Aerogel materials can contain anywhere from 50% to 99.98% air by volume, but in reality, most aerogels exhibit porosity between 90% and 99.8%. Aerogel is produced by extracting the liquid component of the gel through supercritical drying or freeze-drying. This allows the liquid to dry slowly without the solid matrix of the gel collapsing due to capillary action, as occurs with conventional evaporation. Aerogels can be made of a wide variety of substances, including silica, metal oxides, organic polymers, biological polymers, quantum dots, carbon, and metals. Silica aerogels are the most widely used aerogels that consist of a three-dimensional network of connected silica nanoparticles. Because of their remarkable properties, such as high porosity, large surface area, ultra-low bulk density, extremely low thermal conductivity, and high optical transparency in the visible region [3–7], they are useful for thermal insulation [8,9], catalysts [10,11],

sensors [12,13], and environmental remediation [14]. Many of their properties exhibit scope for improvement and new functionalities through surface modification via the introduction of specific functional species [15]. Accordingly, silica aerogels have been commonly used to create a variety of functional composite materials through this approach.

Porphyrins are a class of compounds characterized by a unique macrocyclic structure known as a porphyrin ring. The porphyrin ring structure consists of four pyrrole subunits linked by methine ($-\text{CH}=\text{}$) bridges. The core 16-membered ring with 18 π electrons constitutes unique electronic features that are responsible for its optical properties. This cyclic arrangement also creates a large planar aromatic structure with a central cavity that can accommodate a variety of metal ions. In nature, porphyrin-related compounds such as chlorophylls are essential for the photosynthetic process, as they play a crucial role in capturing and harvesting solar energy and transferring charge/energy for photosynthesis through their molecular assemblies [16]. Porphyrinoids (free-base porphyrins and metalloporphyrins) are among the most prominent molecular components for optoelectronic active materials owing to their extensive capacity to absorb visible light. Porphyrinoids have high absorption coefficients in the regions of 400–440 nm (Soret band) and 500–720 nm (Q bands). Furthermore, unique electronic properties of their aromatic skeletons, robust structural frameworks, and considerable flexibility in molecular design are attractive advantages for the development of a variety of materials [17–21]. Owing to these properties, porphyrinoid-based nano- or micro-structured materials are drawing attention in various fields such as photocatalysis [22], solar energy conversion [23], molecular recognition [24], and biomedical applications [25].

Photocatalysis is increasingly being emphasized as an environmentally friendly process for decomposing organic pollutants in polluted water and air. It is well-documented that porphyrins and metalloporphyrins contribute significantly to photooxidation catalysis [26]. Despite the feasibility, homogeneous porphyrin photocatalysts have not been practically commercialized. They tend to be deactivated via photobleaching or solvolysis by solvents, and their recovery from the reaction medium usually poses additional difficulties. In this case, heterogenization of the porphyrin appears to be necessary. One possible solution is immobilization on organic or inorganic solid supports for improved stability and easy recovery. Grafting porphyrin molecules into a solid matrix is a useful and practical approach to perform the reaction. This is because solid photocatalysts can be easily separated from the reaction medium and reused. Immobilization can improve the stability of catalysts and reduce efficiency losses. Readily available silica has been extensively used as a host for porphyrins [27]. Clay, zeolites, or layered materials can be also involved in accommodating porphyrins [28,29]. To achieve high retention, porphyrins have been shown to be incorporated inside the solid polymer backbone, imparting interesting modifications to their photochemical properties [30]. For heterogenization, more consideration has been given to selecting π -conjugated carbon materials such as carbon nanotubes (CNTs), graphene, or C_3N_4 as supports. As a result, the electron-accepting properties provide opportunities to promote electron transfer and improve photoconversion efficiency [31,32].

On the other hand, nanostructured porphyrins are expected to have significantly different chemical activities and stabilities than free or supported porphyrins [33,34]. In particular, the synthetic versatility allows one to organize porphyrins with control into well-defined nanostructures through supramolecular assembly [35,36]. Porphyrinoids assemble through various supramolecular interactions, such as hydrogen bonding, π - π stacking, metal–ligand coordination, and electrostatic interactions. Hydrophobic and hydrophilic effects further contribute to the self-organization of porphyrinoids in solution [37–40]. There are a variety of methods to fabricate nanostructured porphyrin materials, including surfactant assistance [41], ionic assembly [42], sonication [43], metal–ligand coordination [44], and reprecipitation [45]. For example, π - π interaction was used to form nanorods of 5,15-bis(3,5-di-*tert*-butylphenyl)porphyrin [46]. Intermolecular interactions can be manipulated by fine-tuning the molecular packing mode by appropriately modifying the peripheral position or ring cavity of the porphyrin. These strategies allow one to build rich

and diverse nanostructures of various sizes and shapes. Comprehensive studies have been conducted on how to prepare porphyrin nanostructures using various synthetic methods with various morphology ranges. Methods for synthesizing porphyrin nanomaterials or nanocomposites have been reported to improve photocatalytic performance [47–50].

We have focused on porous composites containing Sn(IV)porphyrins. Sn(IV)porphyrins form stable six-coordinate complexes with two oxyanionic ligands in axial positions owing to the robust oxophilic nature of the Sn(IV) center [51,52]. This favorable coordination of Sn(IV)porphyrins was utilized to fabricate functional porous materials, including a coordination framework [53], multiporphyrin array [54], organic polymer [55], and mesoporous platform [56]. These Sn(IV)porphyrin-containing porous materials exhibit excellent physicochemical stability and remarkable photocatalytic activity for the degradation of organic dyes in aqueous solutions. In particular, the incorporation of Sn(IV)porphyrins to the mesoporous silica (Mobil Composition of Matter No. 41, MCM-41) not only enables the surface modification, but also improves the photocatalytic performance for the degradation of organic pollutants compared with parent Sn(IV)porphyrins. Additionally, nanostructured materials based on Sn(IV)porphyrins yield excellent visible light-activated photocatalytic performance in hydrogen production [57] and organic pollutant degradation [58]. Optoelectronic functional composite materials with porous structures are of great importance in various fields. In this context, we here report the fabrication and characterization of a Sn(IV)porphyrin-embedded silica aerogel composite and its potential for the photolysis of acid orange 7 (AO7) dye. AO7 dye was chosen as a target pollutant because it is nonbiodegradable, chemically stable, mutagenic, and potentially carcinogenic. Water-soluble dyes have been commonly used in the paper printing, textile, and leather industries, where significant quantities are released into the environment. These dyes must be removed from wastewater, as this results in undesirable water pollution.

2. Materials and Methods

Sodium silicate and Amberlite IR-120H ion-exchange resin were purchased from Daejung Chemicals & Metals Company (Seoul, Republic of Korea). Hexamethyldisilazane (HMDS) was purchased from Sigma-Aldrich. All commercial chemicals were used without further purification. (*Trans*-dihydroxo)(5,10,15,20-tetraphenylporphyrinato)tin(IV) (SnP) was similarly prepared according to the reported procedure [59]. Fourier-transform infrared (FT-IR) spectra were acquired using a Shimadzu FTIR-8400S spectrophotometer (Shimadzu, Tokyo, Japan). Steady-state ultraviolet–visible (UV–vis) spectra were recorded using a Shimadzu UV-3600 spectrophotometer (Shimadzu, Tokyo, Japan). Fluorescence spectra were recorded using a Shimadzu RF-5301PC fluorescence spectrophotometer (Shimadzu, Tokyo, Japan). Inductively coupled plasma (ICP) analysis was performed using an ICP-Spectrociros CCD instrument. Zeta potentials were measured using an Otsuka Electronics ELSZ-2. Thermogravimetric analysis (TGA) was performed using an Auto-TGA Q500 instrument (TA Instruments, New Castle, DE, USA). The Brunauer–Emmett–Teller (BET) surface area was determined using an analyzer (BELSORP-mini volumetric adsorption equipment) through N₂ adsorption isotherms at 77 K. The surface area and porous size were estimated using an Autosorb-iQ and Quadrasorb SI. Field-emission scanning electron microscopy (FE-SEM) and transmission electron microscopy (TEM) images were acquired using a MAIA III (TESCAN, Brno, Czech Republic) and JEOL/JEM 2100, respectively.

2.1. Fabrication of SnP@SiA

An aqueous solution of sodium silicate (8 wt%) was passed through a column filled with Amberlite IR-120H ion-exchange resin to replace Na⁺ ions with H⁺ ions. The pH of the resultant silicate solution was adjusted from 3.5 to 4.5 using 1 M ammonia solution. The silicate solution was transferred to a column-shaped mold and gelled at 50 °C for 1 h. Thereafter, the wet gel was soaked in water at 50 °C for 3 days and then washed with distilled water 3 times a day to remove unreacted silicate and excess ammonia. The hydrogel was immersed in an ethanol solution at 50 °C for 1 day to exchange water in the

hydrogel with ethanol and reinforce the gel network. The wet gel was further treated with dichloromethane at room temperature through the same procedure. Subsequently, the gel was placed in a dichloromethane solution containing HDMS (10 v% of dichloromethane) and Sn(OH)₂ TPP (0.01 mol% of HMDS) for 3 days. Afterwards, the gel was colored purple and the dichloromethane solution turned colorless. The purple gel was further treated with *n*-hexane for a day to exchange solvent. The isolated purple gel from *n*-hexane was subject to a supercritical CO₂ atmosphere (at 35 °C and under a pressure of 100 bar) for 4 h. The heating source was removed and CO₂ was slowly depressurized to prevent deformation. The product was further dried at 150 °C under vacuum.

2.2. Preparation of SiA

An aqueous solution of sodium silicate (8 wt%) was passed through a column filled with Amberlite IR-120H ion-exchange resin to replace Na⁺ ions with H⁺ ions. The pH of the resultant silicate solution was adjusted from 3.5 to 4.5 using 1 M ammonia solution. The silicate solution was transferred to a column-shaped mold and gelled at 50 °C for 1 h. Thereafter, the wet gel was soaked in water at 50 °C for 3 days and then washed with distilled water 3 times a day to remove unreacted silicate and excess ammonia. The hydrogel was immersed in an ethanol solution at 50 °C for 1 day to exchange water in the hydrogel with ethanol and reinforce the gel network. The wet gel was further treated with dichloromethane and *n*-hexane successively at room temperature through the same procedure. The isolated gel from *n*-hexane was subject to a supercritical CO₂ atmosphere (at 35 °C and under a pressure of 100 bar) for 4 h. The heating source was removed and CO₂ was slowly depressurized to prevent deformation. The product was further dried at 150 °C under vacuum.

2.3. Preparation of TMS@SiA

An aqueous solution of sodium silicate (8 wt%) was passed through a column filled with Amberlite IR-120H ion-exchange resin to replace Na⁺ ions with H⁺ ions. The pH of the resultant silicate solution was adjusted from 3.5 to 4.5 using 1 M ammonia solution. The silicate solution was transferred to a column-shaped mold and gelled at 50 °C for 1 h. Thereafter, the wet gel was soaked in water at 50 °C for 3 days and then washed with distilled water 3 times a day to remove unreacted silicate and excess ammonia. The hydrogel was immersed in an ethanol solution at 50 °C for 1 day to exchange water in the hydrogel with ethanol and reinforce the gel network. The wet gel was further treated with dichloromethane at room temperature through the same procedure. Subsequently, the gel was placed in a dichloromethane solution containing HDMS (10 v% of dichloromethane) for 3 days. The gel was further treated with *n*-hexane for a day to exchange solvent. The isolated gel from *n*-hexane was subject to a supercritical CO₂ atmosphere (at 35 °C and under a pressure of 100 bar) for 4 h. The heating source was removed and CO₂ was slowly depressurized to prevent deformation. The product was further dried at 150 °C under vacuum.

2.4. Photocatalytic Degradation Experiment

The photocatalytic efficiency of SnP@SiA was evaluated using photodegrading acid orange 7 (AO7) dye in an aqueous solution. Following a typical procedure, 20 mg of SnP@SiA was added to 250 mL of an aqueous solution of AO7 (20 mg L⁻¹, distilled water with pH of 7.0) with stirring at 298 K. The reaction mixture was left to stand in the dark for 30 min to reach the adsorption–desorption equilibrium. Afterward, the irradiation process was started using a 150 W xenon arc lamp with a UV cut-off filter (ABET Technologies, Old Gate Lane Milford, CT, USA) at 298 K. After irradiation with visible light, a 3 mL suspension was collected at regular intervals. The photocatalyst was separated from the solution via centrifugation and collected via filtration using a filter paper. The concentration of AO was determined by measuring the absorbance at 485 nm using a UV–vis spectrophotometer.

3. Results and Discussion

In the fabrication of the targeting material, the coordination chemistry of Sn(IV)porphyrins was utilized to form the hybrid composite silica aerogel. A hybrid composite (SnP@SiA) composed of Sn(IV)porphyrin (SnP) in silica aerogel (SiA) was successfully fabricated through the reaction of SnP with silanol groups of SiA in the presence of hexamethyldisilazane (HMDS), as illustrated in Figure 1. Following a typical procedure, a mixture of SnP and HMDS was reacted with wet SiA in dichloromethane at room temperature. Subsequently, aerogel SnP@SiA with high porosity was extracted from purple-colored wet SnP@SiA gel using supercritical CO₂. The condensation of the axial hydroxo ligand of SnP with a silanol group on the silica surface forms Sn–O–Si chemical bonds in the fabrication of the hybrid composite. HMDS also reacts with the naked hydroxo ligand of SnP and silano groups on the silica surface to form Sn–O–SiMe₃ and Si–O–SiMe₃, respectively. The formation of Sn–O–SiMe₃ was confirmed through a model reaction of HMDS with SnP via ¹H NMR spectroscopy. The resonance of SiMe₃ appeared with an upfield chemical shift value of –3.04 ppm, which was considerably higher than that of HMDS (0.04 ppm) (Figure S1). This upfield shift due to the porphyrin ring-current effect confirms that the axial hydroxo ligand of SnP reacts with HMDS to form a (Me₃SiO)₂Sn(IV)porphyrin complex. The corresponding transformation is shown in Scheme S1. Consequently, SnP@SiA exhibits a more hydrophobic surface composed of Me₃Si–O–SnP–O–Si and Me₃Si–O–Si moieties than unmodified aerogel SiA.

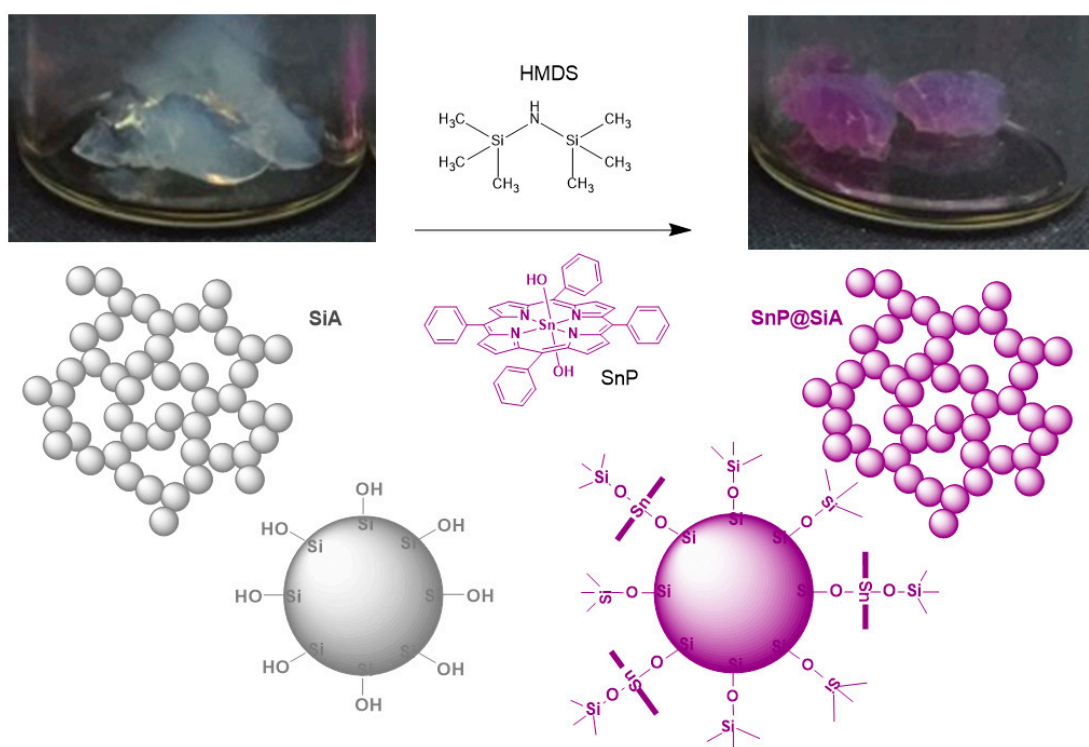


Figure 1. Schematic of SnP@SiA fabrication and photographs of SiA and SnP@SiA specimens.

During the experiments, we made certain useful observations to optimize the reaction condition in terms of solvent system and additive. When the water in the initially formed silica hydrogel is exchanged for an organic solvent, the solvent should be treated in a stepwise manner from less hydrophilic to more hydrophobic. For example, shrinkage and deformation of the wet gel could be prevented through sequential solvent exchange with ethanol, dichloromethane, and *n*-hexane. In the case of ethanol, there was no shrinkage of the wet gel during solvent replacement, but in the case of isopropyl alcohol, the wet gel shrank by approximately 30%. As a solvent that does not affect gelation and readily dissolves SnP, dichloromethane was considerably more effective than toluene and tetrahydrofuran (THF). In contrast, additives are needed to make the surface of silica hydrophobic

and preserve its porous structure without shrinkage during supercritical CO₂ extraction. To this end, trimethylchlorosilane (TMCS) and HMDS were examined as surface modification additives. HMDS developed a hydrophobic surface relatively efficiently without evolving corrosive byproducts such as HCl in the case of TMCS. To determine the effect of the order of surface modification processes, the order of HMDS and SnP treatment was varied during the experiment. When SnP was processed after HMDS treatment, the SnP in silica gel was removed during washing, and when HMDS processing followed that of SnP, silica aerogel with a non-uniformly modified surface was produced. Based on the experiment results, the most optimized SnP@SiA is obtained when SnP and HMDS are simultaneously processed.

Surface modification was characterized by zeta potentials determined using the degree of electrostatic repulsion of the surface. The average zeta potential of SnP@SiA was estimated to be -11.62 mV, which is less negative than that for SiA (-18.26 mV), indicating that the surface of SnP@SiA is covered by hydrophobic species such as SnP and trimethylsilyl groups from HMDS. To examine the thermal decomposition characteristics of SnP@SiA, thermogravimetric analysis (TGA) was performed up to 800 °C. TGA curves for the materials are presented in Figure S2. The SnP@SiA sample obtained via treatment with HMDS and 0.01 mol% SnP showed a total weight loss of 15.7% . The SiA sample exhibited a total weight loss of 2.6% . Based on these results, the total estimated contents of organic substances, including SnP and trimethylsilyl moieties in the sample of SnP@SiA, was approximately 13.1 wt%. The amount of adsorbed SnP was also estimated based on the tin content of SnP@SiA obtained from the treatment of HMDS and 0.01 mol% SnP measured via ICP analysis. The chemically adsorbed amount of SnP in SnP@SiA was estimated to be 0.016 mmol/g.

Fourier-transform infrared (FT-IR) spectra of SnP, SiA, and SnP@SiA are compared in Figures 2 and S3. The FT-IR spectra of SiA and SnP@SiA are very similar to each other. Three characteristic bands for the SiO₂-based materials were observed in both aerogels. The bands at 1085 and 800 cm⁻¹ correspond to Si–O–Si stretching, while the band at 959 cm⁻¹ is assigned to the bending of Si–O–Si for SiA. For SnP@SiA, a shoulder band at 1258 cm⁻¹, a band at 848 cm⁻¹, and a band at 760 cm⁻¹, indicating the presence of trimethylsilyl (TMS; $-\text{Si}(\text{CH}_3)_3$) group, were observed. These characteristic peaks were similarly observed in the silica aerogel sample treated with HMDS (TMS@SiA). It is known that the trimethylsilyl (TMS) group is generally recognized as a band at about 1250 cm⁻¹ along with one or more bands in the range of 865 – 750 cm⁻¹ [60]. Additionally, as shown in Figure S3, the C–H stretching signal for the TMS groups was similarly observed around 2960 cm⁻¹ from SnP@SiA and TMS@SiA samples. Therefore, it was confirmed that the surface of SnP@SiA was covered with hydrophobic Me₃Si–O–SnP–O– and Me₃Si–O– components. Conversely, SnP exhibited numerous bands, such as at 1021 and 796 cm⁻¹, belonging to the bending vibration of C–H and the out-of-plane bending vibration of C–H in the benzene ring, respectively. The bands at 3381 , 1590 , and 1409 cm⁻¹ are attributed to the stretching vibrations of C–H, C=C, and C–N in the pyrrole ring, respectively. However, SnP bands were barely observed for SnP@SiA, probably owing to their considerably low occupancy in the composite.

The optical property of SnP@SiA was investigated using solid-state UV–vis absorption and photoluminescence spectroscopy. SnP@SiA was pelletized with BaSO₄ in the preparation of a solid sample for measurement. Upon being measured, the reflectance of the sample was converted to an absorbance value using the Kubelka–Munk equation. SnP@SiA exhibits robust light absorption at 420 nm owing to the Soret band and three bands at 520 , 560 , and 598 nm, attributed to the Q-bands, as shown in Figure 3a. This observation implies that the Soret band, as well as the Q-bands from the SnP moiety, confirms the strong attachment of SnP in SnP@SiA. In addition, SnP@SiA exhibited an emission band at 649 nm under the excitation light at 560 nm, whereas the emission of solid SnP appeared at 606 and 658 nm (Figure 3b). The emission band patterns for the two materials differ completely, which strongly implies that SnP species in SnP@SiA are well-distributed and closely aggregated with each other in SnP solids.

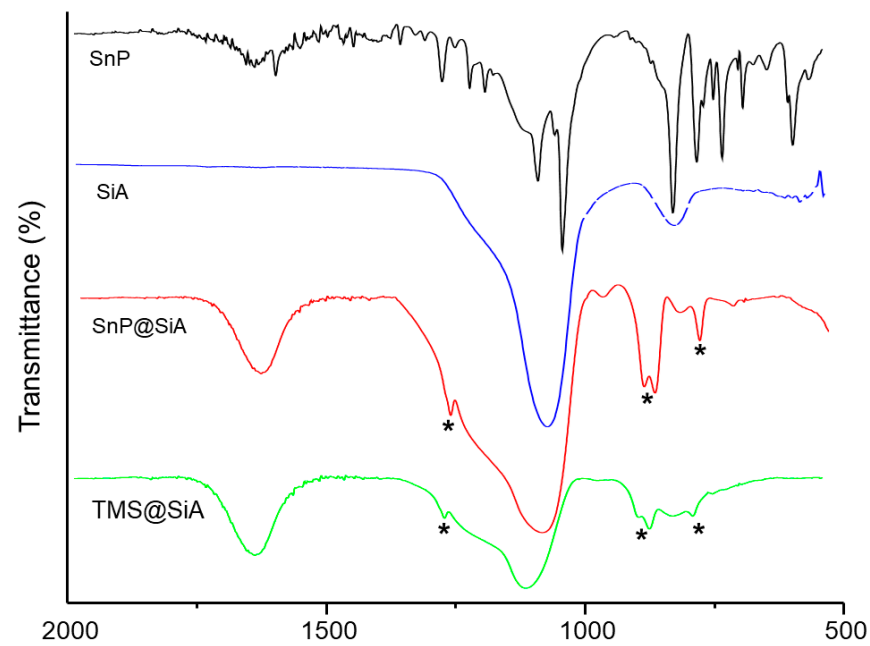


Figure 2. Fourier-transform infrared (FT-IR) spectra of SnP, SiA, SnP@SiA, and TMS@SiA (KBr pellets). The peaks marked with an asterisk (*) are characteristic peaks of $-\text{Si}(\text{CH}_3)_3$ group.

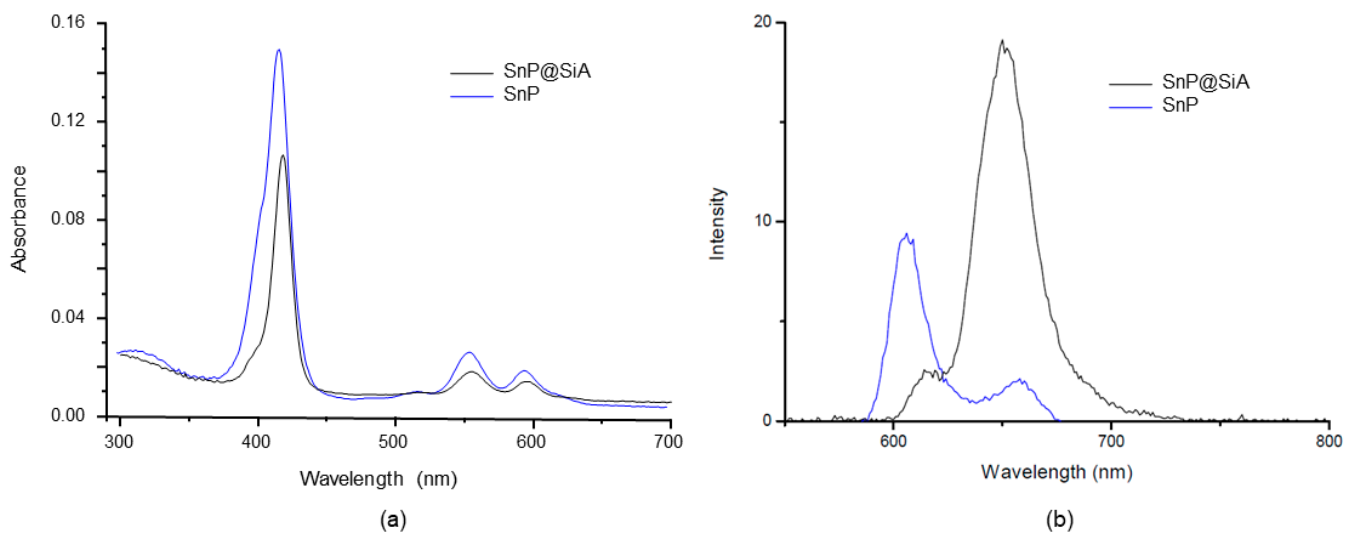


Figure 3. Solid-state UV–vis absorption (a) and photoluminescence (b) spectra of SnP@SiA. In the UV–vis absorption measurement, BaSO_4 pellets were used as sample preparation, and excitation was performed at 560 nm in the photoluminescence measurement.

The structural and morphological development of the fabricated SnP@SiA was investigated using FE-SEM. The FE-SEM image shown in Figure 4a reveals that the SnP@SiA network structure is composed of modified silica nanoparticles with an average diameter of approximately 20 nm. We found that a typical silica aerogel was successfully formed in the fabrication of SnP@SiA. Furthermore, the mesoporous structure of SnP@SiA was confirmed using TEM, as shown in Figure 4b. The nitrogen sorption isotherms for the determination of the permanent porosities of SnP@SiA and SiA were performed. The BET surface area, pore volume, and average pore size of SnP@SiA are $697.07 \text{ m}^2/\text{g}$, $1.69 \text{ cm}^3/\text{g}$, and 8.45 nm , respectively, making the composite suitable for catalytic applications owing to the large available surface. The reductions in the surface area, pore volume, and pore size for SnP@SiA relative to SiA ($939.96 \text{ m}^2/\text{g}$, $2.73 \text{ cm}^3/\text{g}$, and 11.20 nm) evidence the incorporation of SnP and trimethylsilyl species within the mesoporous frameworks. There-

fore, SnP@SiA was successfully coupled with SnP to form a SnP@SiA mesoporous hybrid composite with high porosity and a large surface area.

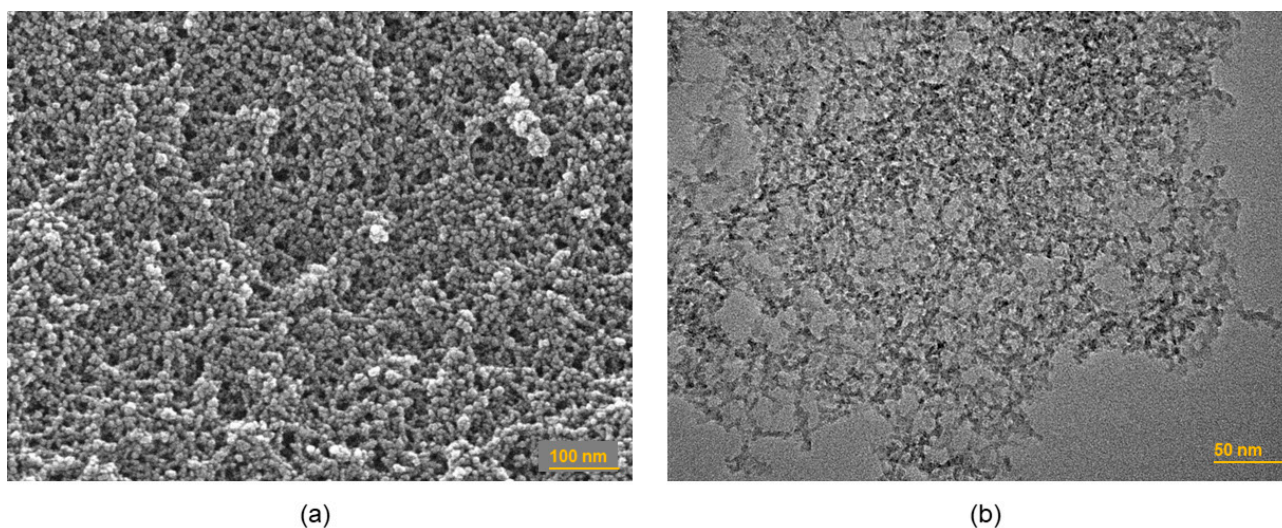


Figure 4. Field-emission scanning electron microscopy (FE-SEM) (a) and transmission electron microscopy (TEM) (b) images of SnP@SiA.

We aimed to use SnP@SiA for environmental applications, such as the photocatalytic degradation of organic pollutants in water, because SnP complexes exhibit outstanding visible-light-activated photocatalytic activity. For this application, the photocatalytic performance of SnP@SiA in the degradation of acid orange 7 (AO7) as a model pollutant dye under visible light irradiation in aqueous solutions was investigated (Figure 5). Negligible decay of AO7 dye was observed in the absence of a photocatalyst or in the presence of SiA, implying that SiA does not work as a photocatalyst under visible light irradiation. However, the absorbance of AO7 dye at 485 nm significantly decreased in the presence of SnP@SiA with the increase in the visible light irradiation time. Therefore, this preliminary study demonstrates that SnP@SiA, a photocatalyst with high porosity and large surface area, exhibits promising performance in the photodegradation of AO7 under visible light irradiation in aqueous solution.

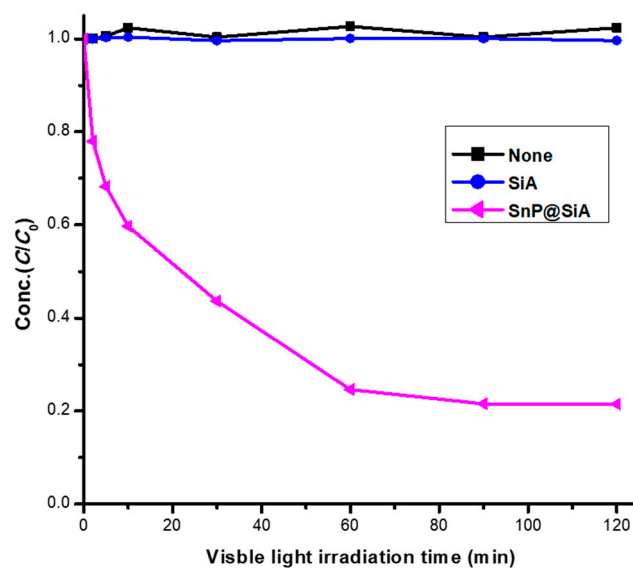


Figure 5. Photocatalytic degradation of AO7 dye in an aqueous solution (pH = 7, T = 298 K) under visible light irradiation in the presence of SiA and SnP@SiA.

4. Conclusions

A hybrid composite (SnP@SiA) composed of (*trans*-dihydroxo)(5,10,15,20-tetraphenylporphyrinato)tin(IV) (SnP) in silica aerogel (SiA) was successfully fabricated through the reaction of SnP with silanol groups of SiA in the presence of hexamethyldisilazane (HMDS). In the fabrication of the targeting material, the coordination chemistry of Sn(IV)porphyrins was utilized to form the hybrid composite silica aerogel. Thus, this work provides an efficient strategy for developing functional silica aerogels. SnP@SiA was characterized using various instrumental techniques. Surface modification was particularly characterized by zeta potentials and FT-IR spectroscopy, which confirmed that the surface of SnP@SiA was covered with hydrophobic Me₃Si–O–SnP–O– and Me₃Si–O– components. SnP@SiA was strongly coupled with SnP to form the SnP@SiA mesoporous hybrid composite, a photocatalyst with high porosity and a large surface area that exhibited promising performance in the photodegradation of acid orange 7 (AO7) under visible light irradiation in aqueous solution. The hybrid composite SnP@SiA exhibited the desirable properties of aerogels along with photoelectronic features of porphyrins. This class of porphyrin-embedded porous materials has valuable potential in various applications such as photocatalysis, light energy conversion, biochemical sensors, and gas storage.

Supplementary Materials: The following supporting information can be downloaded at: <https://www.mdpi.com/article/10.3390/jcs7090401/s1>, Scheme S1: Chemical reaction of SnP with HMDS; Figure S1: ¹H NMR spectrum for the reaction of SnP with HMDS in CDCl₃; Figure S2: TGA curves for SnP (a), SiA (b), and SnP@SiA (c); Figure S3: FT-IR spectra of SnP, SiA, SnP@SiA, and TMS@SiA (KBr pellets).

Author Contributions: Methodology, software, formal analysis, investigation, data curation, visualization, M.-G.J. and N.-G.K.; conceptualization, funding acquisition, project administration, supervision, validation, resources, writing—original draft preparation, review and editing, H.-J.K. All authors have read and agreed to the published version of the manuscript.

Funding: This study was supported by the National Research Foundation of Korea (grant no. 2022R1F1A1074420) funded by the Korean government (MSIT).

Data Availability Statement: Not applicable.

Conflicts of Interest: The authors declare no conflict of interest.

References

1. Hüsing, N.; Schubert, U. Aerogels—Airy materials: Chemistry, structure, and properties. *Angew. Chem. Int. Ed.* **1998**, *37*, 22–45. [[CrossRef](#)]
2. Pierre, A.C.; Pajonk, G.M. Chemistry of Aerogels and Their Applications. *Chem. Rev.* **2002**, *102*, 4243–4265. [[CrossRef](#)] [[PubMed](#)]
3. Sonu, S.S.; Rai, N.; Chauhan, I. Multifunctional Aerogels: A comprehensive review on types, synthesis and applications of aerogels. *J. Sol-Gel Sci. Technol.* **2023**, *105*, 324–336.
4. Du, A.; Zhou, B.; Zhang, Z.; Shen, J. A Special Material or a New State of Matter: A Review and Reconsideration of the Aerogel. *Materials* **2013**, *6*, 941–968. [[CrossRef](#)]
5. Akhter, F.; Soomro, S.A.; Inglezakis, V.J. Silica aerogels; a review of synthesis, applications and fabrication of hybrid composites. *J. Porous Mater.* **2021**, *28*, 1387–1400. [[CrossRef](#)]
6. Meti, P.; Wang, Q.; Mahadik, D.B.; Lee, K.-Y.; Gong, Y.-D.; Park, H.-H. Evolutionary Progress of Silica Aerogels and Their Classification Based on Composition: An Overview. *Nanomaterials* **2023**, *13*, 1498. [[CrossRef](#)]
7. Noman, M.T.; Amor, N.; Ali, A.; Petrik, S.; Coufal, R.; Adach, K.; Fijalkowski, M. Aerogels for Biomedical, Energy and Sensing Applications. *Gels* **2021**, *7*, 264. [[CrossRef](#)]
8. Merillas, B.; Vareda, J.P.; Martín-de León, J.; Rodríguez-Pérez, M.Á.; Durães, L. Thermal Conductivity of Nanoporous Materials: Where Is the Limit? *Polymers* **2022**, *14*, 2556. [[CrossRef](#)]
9. Bandi, S.; Bell, M.; Schiraldi, D.A. Temperature-responsive clay aerogel—polymer composites. *Macromolecules* **2005**, *38*, 9216–9220. [[CrossRef](#)]
10. Asmussen, R.M.; Matyáš, J.; Qafoku, N.P.; Kruger, A.A. Silver-functionalized silica aerogels and their application in the removal of iodine from aqueous environments. *J. Hazard. Mater.* **2019**, *379*, 119364. [[CrossRef](#)]
11. Noman, M.T.; Amor, N.; Petru, M.; Mahmood, A.; Kejzlar, P. Photocatalytic Behaviour of Zinc Oxide Nanostructures on Surface Activation of Polymeric Fibres. *Polymers* **2021**, *13*, 1227. [[CrossRef](#)] [[PubMed](#)]

12. Ahmad, V.; Ahmad, A.; Khan, S.A.; Ahmad, A.; Abuzinadah, M.F.; Karim, S.; Jamal, Q.M.S. Biomedical applications of aerogel. In *Advances in Aerogel Composites for Environmental Remediation*; Elsevier: Amsterdam, The Netherlands, 2021; pp. 33–48.
13. Siddique, J.A.; Ansari, S.P.; Yadav, M. Carbon aerogel composites for gas sensing. In *Advances in Aerogel Composites for Environmental Remediation*; Elsevier: Amsterdam, The Netherlands, 2021; pp. 49–73.
14. Ansari, S.P.; Husain, A.; Shariq, M.U.; Ansari, M.O. Conducting polymer-based aerogels for energy and environmental remediation. In *Advances in Aerogel Composites for Environmental Remediation*; Elsevier: Amsterdam, The Netherlands, 2021; pp. 75–86.
15. Li, Z.; Zhao, S.; Koebel, M.K.; Malfait, W.J. Silica aerogels with tailored chemical functionality. *Mater. Des.* **2020**, *193*, 108833. [[CrossRef](#)]
16. Hori, T.; Aratani, N.; Takagi, A.; Matsumoto, T.; Kawai, T.; Yoon, M.-C.; Yoon, Z.C.; Cho, S.; Kim, D.; Osuka, A. Giant Porphyrin Wheels with Large Electronic Coupling as Models of Light-Harvesting Photosynthetic Antenna. *Chem. Eur. J.* **2006**, *12*, 1319–1327. [[CrossRef](#)] [[PubMed](#)]
17. Drain, C.M.; Hupp, J.T.; Suslick, K.S.; Wasielewski, M.R.; Chen, X. A perspective on four new porphyrin-based functional materials and devices. *J. Porphyr. Phthalocyanines* **2002**, *6*, 243–258. [[CrossRef](#)]
18. Milic, T.N.; Chi, N.; Yablon, D.G.; Flynn, G.W.; Batteas, J.D.; Drain, C.M. Controlled hierarchical self-assembly and deposition of nanoscale photonic materials. *Angew. Chem. Int. Ed.* **2002**, *41*, 2117–2119. [[CrossRef](#)]
19. Suslick, K.S.; Rakow, N.A.; Kosal, M.E.; Chou, J.-H. The materials chemistry of porphyrins and metalloporphyrins. *J. Porphyr. Phthalocyanines* **2000**, *4*, 407–413. [[CrossRef](#)]
20. Chou, J.-H.; Nalwa, H.S.; Kosal, M.E.; Rakow, N.A.; Suslick, K.S. Applications of Porphyrins and Metalloporphyrins to Materials Chemistry. In *The Porphyrin Handbook*; Kadish, K.M., Smith, K.M., Guillard, R., Eds.; Academic Press: San Diego, CA, USA, 2000; Volume 6, pp. 43–131.
21. Hasobe, T. Photo- and electro-functional self-assembled architectures of porphyrins. *Phys. Chem. Chem. Phys.* **2012**, *14*, 15975–15987. [[CrossRef](#)]
22. Nikolaou, V.; Charalambidis, G.; Coutsolelos, A.G. Photocatalytic hydrogen production of porphyrin nanostructures: Spheres vs. fibrils, a case study. *Chem. Commun.* **2021**, *57*, 4055–4058. [[CrossRef](#)]
23. Zhang, Q.; Uchaker, E.; Candelaria, S.L.; Cao, G. Nanomaterials for Energy Conversion and Storage. *Chem. Soc. Rev.* **2013**, *42*, 3127–3171. [[CrossRef](#)]
24. Farinone, M.; Urbańska, K.; Pawlicki, M. BODIPY- and Porphyrin-Based Sensors for Recognition of Amino Acids and Their Derivatives. *Molecules* **2020**, *25*, 4523. [[CrossRef](#)]
25. Grigore, M.E.; Ion, R.-M.; Iancu, L. Tailored porphyrin–gold nanoparticles for biomedical applications. *J. Porphyr. Phthalocyanines* **2019**, *23*, 766–780. [[CrossRef](#)]
26. Chen, Y.; Huang, Z.-H.; Wang, L.-N. Porphyrin-Based Organophotocatalysts. In *Phthalocyanines and Some Current Applications*; Yilmaz, Y., Ed.; IntechOpen: London, UK, 2017; Chapter 6; pp. 119–151.
27. Ribeiro, S.M.; Serra, A.C.; Gonsalves, A.M.A.R. Covalently immobilized porphyrins on silica modified structures as photooxidation catalysts. *J. Mol. Catal. A* **2010**, *326*, 121–127. [[CrossRef](#)]
28. Bedioui, F. Zeolite-encapsulated and clay-intercalated metal porphyrin, phthalocyanine and Schiff-base complexes as models for biomimetic oxidation catalysts: An overview. *Coord. Chem. Rev.* **1995**, *144*, 39–68. [[CrossRef](#)]
29. Skrobot, F.; Valente, A.; Neves, G.; Rosa, I.; Rocha, J.; Cavaleiro, J. Monoterpenes oxidation in the presence of Y zeolite-entrapped manganese (III) tetra (4-N-benzylpyridyl) porphyrin. *J. Mol. Catal. A* **2003**, *201*, 211–222. [[CrossRef](#)]
30. Maldotti, A.; Molinari, A.; Andreotti, L.; Fogagnolo, M.; Amadelli, R. Novel reactivity of photoexcited iron porphyrins caged into a polyfluoro sulfonated membrane in catalytic hydrocarbon oxygenation. *Chem. Commun.* **1998**, 507–508. [[CrossRef](#)]
31. Baskaran, D.; Mays, J.W.; Zhang, X.P.; Bratcher, M.S. Carbon Nanotubes with Covalently Linked Porphyrin Antennae: Photoinduced Electron Transfer. *J. Am. Chem. Soc.* **2005**, *127*, 6916–6917. [[CrossRef](#)]
32. Chen, D.; Wang, K.; Hong, W.; Zong, R.; Yao, W.; Zhu, Y. Visible light photoactivity enhancement via CuTCPP hybridized g-C₃N₄ nanocomposite. *Appl. Catal. B* **2015**, *166*, 366–373. [[CrossRef](#)]
33. Vasilopoulou, M.; Douvas, A.M.; Georgiadou, D.G.; Constantoudis, V.; Davazoglou, D.; Kennou, S.; Palilia, L.C.; Daphnomili, D.; Coutsolelos, A.G.; Argitis, P. Large work function shift of organic semiconductors inducing enhanced interfacial electron transfer in organic optoelectronics enabled by porphyrin aggregated nanostructures. *Nano Res.* **2014**, *7*, 679–693. [[CrossRef](#)]
34. Liu, H.; Xu, J.; Li, Y.; Li, Y. Aggregate Nanostructures of Organic Molecular Materials. *Acc. Chem Res.* **2010**, *43*, 1496–1508. [[CrossRef](#)]
35. Lee, S.J.; Hupp, J.T.; Nguyen, S.T. Growth of Narrowly Dispersed Porphyrin Nanowires and Their Hierarchical Assembly into Macroscopic Columns. *J. Am. Chem. Soc.* **2008**, *130*, 9632–9633. [[CrossRef](#)]
36. Yoon, S.M.; Hwang, I.C.; Kim, K.S.; Choi, H.C. Synthesis of single-crystal tetra (4-pyridyl) porphyrin rectangular nanotubes in the vapor phase. *Angew. Chem. Int. Ed.* **2009**, *48*, 2506–2509. [[CrossRef](#)]
37. Lehn, J.-M. Perspectives in Supramolecular Chemistry—From Molecular Recognition towards Molecular Information Processing and Self-Organization. *Angew. Chem. Int. Ed. Engl.* **1990**, *29*, 1304–1319. [[CrossRef](#)]
38. Beletskaya, I.; Tyurin, V.S.; Tsivadze, A.Y.; Guillard, R.; Stern, C. Supramolecular chemistry of metalloporphyrins. *Chem. Rev.* **2009**, *109*, 1659–1713. [[CrossRef](#)] [[PubMed](#)]
39. Durot, S.; Taesch, J.; Heitz, V. Multiporphyrinic Cages: Architectures and Functions. *Chem. Rev.* **2014**, *114*, 8542–8578. [[CrossRef](#)] [[PubMed](#)]

40. Shao, S.; Rajendiran, V.; Lovell, J.F. Metalloporphyrin nanoparticles: Coordinating diverse theranostic functions. *Coord. Chem. Rev.* **2019**, *379*, 99–120. [[CrossRef](#)]
41. Zhang, C.; Chen, P.; Dong, H.; Zhen, Y.; Liu, M.; Hu, W. Porphyrin Supramolecular 1D Structures via Surfactant-Assisted Self-Assembly. *Adv. Mater.* **2015**, *27*, 5379–5387. [[CrossRef](#)]
42. Wang, Z.; Medforth, C.J.; Shelnut, J.A. Porphyrin Nanotubes by Ionic Self-Assembly. *J. Am. Chem. Soc.* **2004**, *126*, 15954–15955. [[CrossRef](#)] [[PubMed](#)]
43. Riaz, S.; Feng, W.; Khan, A.F.; Nawaz, M.H. Sonication-induced self-assembly of polymeric porphyrin-fullerene: Formation of nanorings. *J. Appl. Polym. Sci.* **2016**, *133*, 43537. [[CrossRef](#)]
44. Maeda, H.; Hasegawa, M.; Hashimoto, T.; Kakimoto, T.; Nishio, S.; Nakanishi, T. Nanoscale Spherical Architectures Fabricated by Metal Coordination of Multiple Dipyrin Moieties. *J. Am. Chem. Soc.* **2006**, *128*, 10024–10025. [[CrossRef](#)] [[PubMed](#)]
45. Gong, X.; Milic, T.; Xu, C.; Batteas, J.D.; Drain, C.M. Preparation and Characterization of Porphyrin Nanoparticles. *J. Am. Chem. Soc.* **2002**, *124*, 14290–14291. [[CrossRef](#)]
46. Hasobe, T.; Oki, H.; Sandanayakaa, A.S.D.; Murata, H. Sonication-assisted supramolecular nanorods of meso-diaryl-substituted porphyrins. *Chem. Commun.* **2008**, 724–726. [[CrossRef](#)]
47. Medforth, C.J.; Wang, Z.; Martin, K.E.; Song, Y.; Jacobsen, J.L.; Shelnut, J.A. Self-assembled porphyrin nanostructures. *Chem. Commun.* **2009**, 7261–7277. [[CrossRef](#)]
48. Guo, P.; Chen, P.; Liu, M. Porphyrin Assemblies via a Surfactant-Assisted Method: From Nanospheres to Nanofibers with Tunable Length. *Langmuir* **2012**, *28*, 15482–15490. [[CrossRef](#)] [[PubMed](#)]
49. Guo, P.; Chen, P.; Ma, W.; Liu, M. Morphology-dependent supramolecular photocatalytic performance of porphyrin nanoassemblies: From molecule to artificial supramolecular nanoantenna. *J. Mater. Chem.* **2012**, *22*, 20243–20249. [[CrossRef](#)]
50. Wang, J.; Zhong, Y.; Wang, L.; Zhang, N.; Cao, R.; Bian, K.; Alarid, L.; Haddad, R.E.; Bai, F.; Fan, H. Morphology-Controlled Synthesis and Metalation of Porphyrin Nanoparticles with Enhanced Photocatalytic Performance. *Nano Lett.* **2016**, *16*, 6523–6528. [[CrossRef](#)] [[PubMed](#)]
51. Sanders, J.K.M.; Bampos, N.; Clyde-Watson, Z.; Darling, S.L.; Hawley, J.C.; Kim, H.-J.; Mak, C.C.; Webb, S.J. Axial Coordination Chemistry of Metalloporphyrins. In *The Porphyrin Handbook*; Kadish, K.M., Smith, K.M., Guillard, R., Eds.; Academic Press: San Diego, CA, USA, 2000; Volume 3, pp. 1–48.
52. Arnold, D.P.; Blok, J. The coordination chemistry of tin porphyrin complexes. *Coord. Chem. Rev.* **2004**, *248*, 299–319. [[CrossRef](#)]
53. Shee, N.K.; Kim, H.-J. Coordination framework materials fabricated by the self-assembly of Sn(IV) porphyrins with Ag(I) ions for the photocatalytic degradation of organic dyes in wastewater. *Inorg. Chem. Front.* **2022**, *9*, 1270–1280. [[CrossRef](#)]
54. Shee, N.K.; Kim, H.-J. Supramolecular squares of Sn(IV) porphyrins with Re(I)-corners for the fabrication of self-assembled nanostructures performing photocatalytic degradation of Eriochrome Black T dye. *Int. J. Mol. Sci.* **2022**, *23*, 13702. [[CrossRef](#)]
55. Lee, C.-J.; Shee, N.K.; Kim, H.-J. Fabrication and Properties of Sn(IV)Porphyrin-Linked Porous Organic Polymer for Environmental Applications. *RSC Adv.* **2023**, *13*, 24077–24085. [[CrossRef](#)]
56. Shee, N.K.; Park, B.-H.; Kim, H.-J. Hybrid Composite of Sn(IV)-Porphyrin and Mesoporous Structure for Enhanced Visible Light Photocatalytic Degradation of Organic Dyes. *Molecules* **2023**, *28*, 1886. [[CrossRef](#)]
57. Kim, S.H.; Kim, H.-J. Photocatalytic Hydrogen Production by the Sensitization of Sn(IV)-Porphyrin Embedded in a Nafion Matrix Coated on TiO₂. *Molecules* **2022**, *27*, 3770. [[CrossRef](#)] [[PubMed](#)]
58. Shee, N.K.; Kim, H.-J. Morphology-controlled self-assembled nanostructures of complementary metalloporphyrin triads through intermolecular coordination tuning and their photocatalytic degradation for Orange II. *Inorg. Chem. Front.* **2022**, *9*, 5538–5548. [[CrossRef](#)]
59. Crossley, M.J.; Thordarson, P.R.; Wu, A.-S. Efficient formation of lipophilic dihydroxotin(IV) porphyrins and bis-porphyrins. *J. Chem. Soc. Perkin Trans.* **2001**, 2294–2302. [[CrossRef](#)]
60. Launer, P.J. Infrared Analysis of Organosilicon Compounds: Spectra-Structure Correlations. In *Silicon Compounds: Silanes & Silicones*; Gelest, Inc.: Morrisville, PA, USA, 2013.

Disclaimer/Publisher's Note: The statements, opinions and data contained in all publications are solely those of the individual author(s) and contributor(s) and not of MDPI and/or the editor(s). MDPI and/or the editor(s) disclaim responsibility for any injury to people or property resulting from any ideas, methods, instructions or products referred to in the content.